NANO · MICRO small
www.small-journal.com

Hierarchically Well-Developed Porous Graphene Nanofibers Comprising N-Doped Graphitic C-Coated Cobalt Oxide Hollow Nanospheres As Anodes for High-Rate Li-Ion Batteries

Jae Seob Lee, Min Su Jo, Rakesh Saroha, Dae Soo Jung, Young Hoe Seon, Jun Su Lee, Yun Chan Kang, Dong-Won Kang,* and Jung Sang Cho**

Hierarchically well-developed porous graphene nanofibers comprising N-doped graphitic C (NGC)-coated cobalt oxide hollow nanospheres are introduced as anodes for high-rate Li-ion batteries. For this, three strategies, comprising the Kirkendall effect, metal–organic frameworks, and compositing with highly conductive C, are applied to the 1D architecture. In particular, NGC layers are coated on cobalt oxide hollow nanospheres as a primary transport path of electrons followed by graphene-nanonetwork-constituting nanofibers as a continuous and secondary electron transport path. Superior cycling performance is achieved, as the unique nanostructure delivers a discharge capacity of 823 mAh g^{-1} after 500 cycles at 3.0 A g^{-1} with a low decay rate of 0.092% per cycle. The rate capability is also noteworthy as the structure exhibits high discharge capacities of 1035, 929, 847, 787, 747, 703, 672, 650, 625, 610, 570, 537, 475, 422, 294, and 222 mAh g^{-1} at current densities of 0.5, 1.5, 3, 5, 7, 10, 12, 15, 18, 20, 25, 30, 40, 50, 80, and 100 A g^{-1}, respectively. In view of the highly efficient Li^+ ion/electron diffusion and high structural stability, the present nanostructuring strategy has a huge potential in opening new frontiers for high-rate and long-lived stable energy storage systems.

1. Introduction

Owing to the high energy density, Li-ion batteries (LIBs) have played an indispensable role in energy storage.[1–4] However, despite the fast development in LIBs, the low-rate capability of current LIBs has limited their use in electric vehicles (EVs), smart grids, and portable power tools that require fast charging and discharging at high power rates.[1–3] To obtain high-rate LIBs, nanostructuring has proven to be an effective strategy for solving the kinetic problems associated with the diffusion of Li^+ ions and transportation of electrons during repeated cycles.[1–4] Consequently, many nanostructures with various compositions have been studied in transitional metal oxides (TMOs) and their carbon composites.[1–3]

The critical aspect in the design of anode materials with high rate performance is the use of functional nanomaterials that possess short and efficient Li^+ ion and electron pathways, share a large contact area with the electrolyte, and can accommodate strain during cycles.[2–4] To address these requirements, three main strategies—the Kirkendall diffusion effect, metal-organic frameworks (MOFs), and compositing with highly conductive C—were applied to the 1D architecture in this study. The Kirkendall effect has been studied to convert solid metals into hollow metal compounds, induced by the difference in diffusion fluxes of atoms at inorganic interfaces.[5,6] When the outward diffusion of one atom is much faster than the inward diffusion of another, vacancies are created and coalesce into voids, resulting in hollow space.[5,6] Hollow metal oxides offer faster diffusion for Li^+ ion insertion/desertion than solid ones and can better tolerate the volume variations associated with the phase transitions that occur during cycling.[6–8]

As a second strategy, MOFs consisting of metal ion nodes and organic linkers are a new class of porous material that offer benefits such as adjustable pore sizes, controllable architectures, and large surface areas.[9–12] By heat treatment under an inert atmosphere, MOFs are transformed into carbon composites with a high surface area and numerous pores, owing to

J. S. Lee, M. S. Jo, Dr. R. Saroha, Y. H. Seon, J. S. Lee, Prof. J. S. Cho
Department of Engineering Chemistry
Chungbuk National University
1, Chungdae-Ro, Seowon-Gu, Cheongju-si, Chungbuk 361-763, Republic of Korea
E-mail: jscho@cbnu.ac.kr
Dr. D. S. Jung
Energy & Environmental Division
Korea Institute of Ceramic Engineering & Technology (KICET)
101 Soho-Ro, Jinju-si, Gyeongsangnam-do 52581, Republic of Korea
Prof. Y. C. Kang
Department of Materials Science and Engineering
Korea University, Anam-Dong
Seongbuk-Gu, Seoul 136-713, Republic of Korea
E-mail: yckang@korea.ac.kr
Prof. D.-W. Kang
School of Energy Systems Engineering
Chung-Ang University
Seoul 06974, Republic of Korea
E-mail: kangdwn@cau.ac.kr
The ORCID identification number(s) for the author(s) of this article can be found under https://doi.org/10.1002/smll.202002213.

DOI: 10.1002/smll.202002213

the carbonization of the organic ligands.[9,10] Therefore, MOF-derived nanostructures share a large contact area with the electrolyte, possess short Li^+ ion and electron pathways, and can accommodate strain during cycling, which benefits LIBs.[9–12] For example, Lou et al. prepared CoS_2/CNT nanocomposite using a two-step method involving metal-organic framework (i.e., ZIF-67) for the formation of hierarchical carbon nanotube frameworks.[11] The resulting CoS_2/CNT nanocomposite exhibits high initial discharge and charge capacity of 1187 and 927 mAh g^{-1}, respectively at 1 A g^{-1} with 78% Coulombic efficiency. The cycling performance was also commendable as the synthesized nanocomposite delivers a high capacity of 937 mAh g^{-1} at 1 A g^{-1} after 160 cycles with 100% Coulombic efficiency due to its fast lithium diffusion process and efficient electrolyte percolation. Similarly, Dong and co-workers reported a facile synthesis approach to obtain porous $NiCo_2O_4$/NiO hollow dodecahedron as a LIB anode material using ZIF-67 as both precursor and self-sacrificing template.[12] The porous $NiCo_2O_4$/NiO-hollow dodecahedron nanostructure results in high initial discharge capacity of ≈1622 mAh g^{-1} at a current density of 0.2 A g^{-1}. Owing to its high electrochemical activity, large surface area, effective tolerance to volumetric expansion during Li-ion insertion, and good conductivity, the synthesized nanostructure reveals outstanding cycling performance (97.2% capacity retention after 100 cycles at 0.2 A g^{-1}) and rate capabilities.

The third strategy implemented to enhance the rate properties of LIBs is compositing TMOs with both graphitic carbon (GC) and graphene with high electrical conductivities. In general, carbon coating on TMOs only provides single-electron pathways surrounding individual particles.[13,14] It leads to poor connectivity between randomly distributed particles, which induces nonconsecutive electron transport pathways and restricts the high-rate property of anodes. Therefore, a more effective design that could offset the defects in carbon coating is necessary. In this study, we coated N-doped GC (NGC) layers onto TMOs for the primary transport path of electrons; then, the NGC-coated TMOs were surrounded by graphene-nanonetwork-constituting nanofibers as a continuous and secondary electron transport path to the current corrector. To the best of our knowledge, graphene-matrixed nanofibers composed with MOF-derived hollow metal oxide nanospheres, resulting from the application of the Kirkendall effect, have not been studied, owing to the absence of an organized strategy.

Thus, we herein designed a new nanostructure named "hierarchical porous graphene nanofibers comprising N-doped graphitic C-coated cobalt oxide hollow nanospheres" by applying the above-mentioned strategies for high-rate LIBs anodes. The obtained functional materials were studied as LIB anodes and found to exhibit excellent cycling stability and exceptional rate capability. The formation mechanism of the nanostructure and its electrochemical properties in LIBs were also studied in detail.

2. Results and Discussion

The hierarchical porous structured rGO matrixed nanofibers comprising hollow cobalt oxide nanospheres coated with NGC were prepared by applying a multistep process to the electrospun nanofibers. The detailed synthetic mechanism for the unique nanostructure is described systematically in **Scheme 1**a. First, as-spun precursor nanofibers composed of $Co(Ac)_2$, GO, PVA, and PS nanobeads were prepared by electrospinning as a self-engaged matrix to supply cobalt for the growth of ZIF-67 nanocrystals on the fiber surface (Scheme 1a-①). Subsequently, owing to the strong coordination of 2-methylimidazole to cobalt ions within the as-spun $Co(Ac)_2$/GO/PVA/PS composite nanofibers in the methanol, ZIF-67 nanocrystals were uniformly grown on the surface of the nanofibers (Scheme 1a-②). Therefore, $Co(Ac)_2$/GO/PVP/PS nanofibers coated with ZIF-67 nanocrystals could be obtained. After the first heat-treatment under a reducing atmosphere (H_2/Ar = 5/95 (v:v)), ZIF-67 nanocrystals were converted into metallic Co/NGC composite nanocrystals. Thus formed metallic Co particles further acted as a catalyst for the graphitization of carbon.[9,10] As a result, the amorphous carbon (AC) around the Co metals was graphitized into graphitic carbon (GC). At the same time, the N-rich organic ligands of the ZIF-67 crystals were presumed to act as the N doping source,[9,10] such that N was doped into the GC structure to form N-doped GC (NGC). Therefore, the metallic Co nanosphere was coated with NGC (Scheme 1a-③). During reduction, both GO-matrixed nanofibers were reduced into reduced-GO (rGO), and the uniformly distributed PS nanobeads were decomposed into a gaseous product, resulting in the formation of numerous pores in the rGO matrix. In particular, the pores can enable the efficient infiltration of reducing gas inside the rGO-matrixed structure, resulting in the formation of uniformly distributed nanosized metallic Co particles. By applying the nanoscale Kirkendall diffusion strategy in an oxidizing atmosphere (Scheme 1a-④), Co solid metals were converted into cobalt oxide hollow nanospheres. The detail Kirkendall diffusion mechanism was described in Scheme S1 (Supporting Information). The surface oxidation of metallic Co formed a Co/cobalt oxide core–shell structure (Scheme S1-②, Supporting Information). Co^{3+} and Co^{2+} cations diffused outward more quickly than the inward diffusion of oxygen, consistent with the larger ionic radius of O^{2-} anions (140 pm) compared to Co^{3+} cations (61 pm) and Co^{2+} cations (74.5 pm). Accordingly, Kirkendall voids were generated near the Co/cobalt oxide interface during the vacancy-assisted exchange of materials via bulk interdiffusion(Scheme S1-③, Supporting Information). The complete conversion of Co metal into cobalt oxide by nanoscale Kirkendall diffusion resulted in the formation of hollow cobalt oxide nanopowder (Scheme 1a-④ and Scheme S1-④, Supporting Information). In particular, the hollow cobalt oxide nanospheres were coated with an NGC layer with high electrical conductivity. Therefore, the hollow cobalt oxide@NGC particles with enhanced electrical conductivity could primarily serve as fast and continuous transport pathways for electrons (Scheme 1b-①,②), which were subsequently transferred to secondary pathways composed of an rGO-network nanofiber matrix during cycling, as shown in Scheme 1b-③.

The formation mechanism of the hierarchical porous rGO matrixed nanofibers comprising hollow NGC-coated cobalt oxide nanospheres as anode was elucidated by an investigation of the morphological and phase changes of the nanofibers at each process. As-stabilized $Co(Ac)_2$/GO/PVA/PS composite

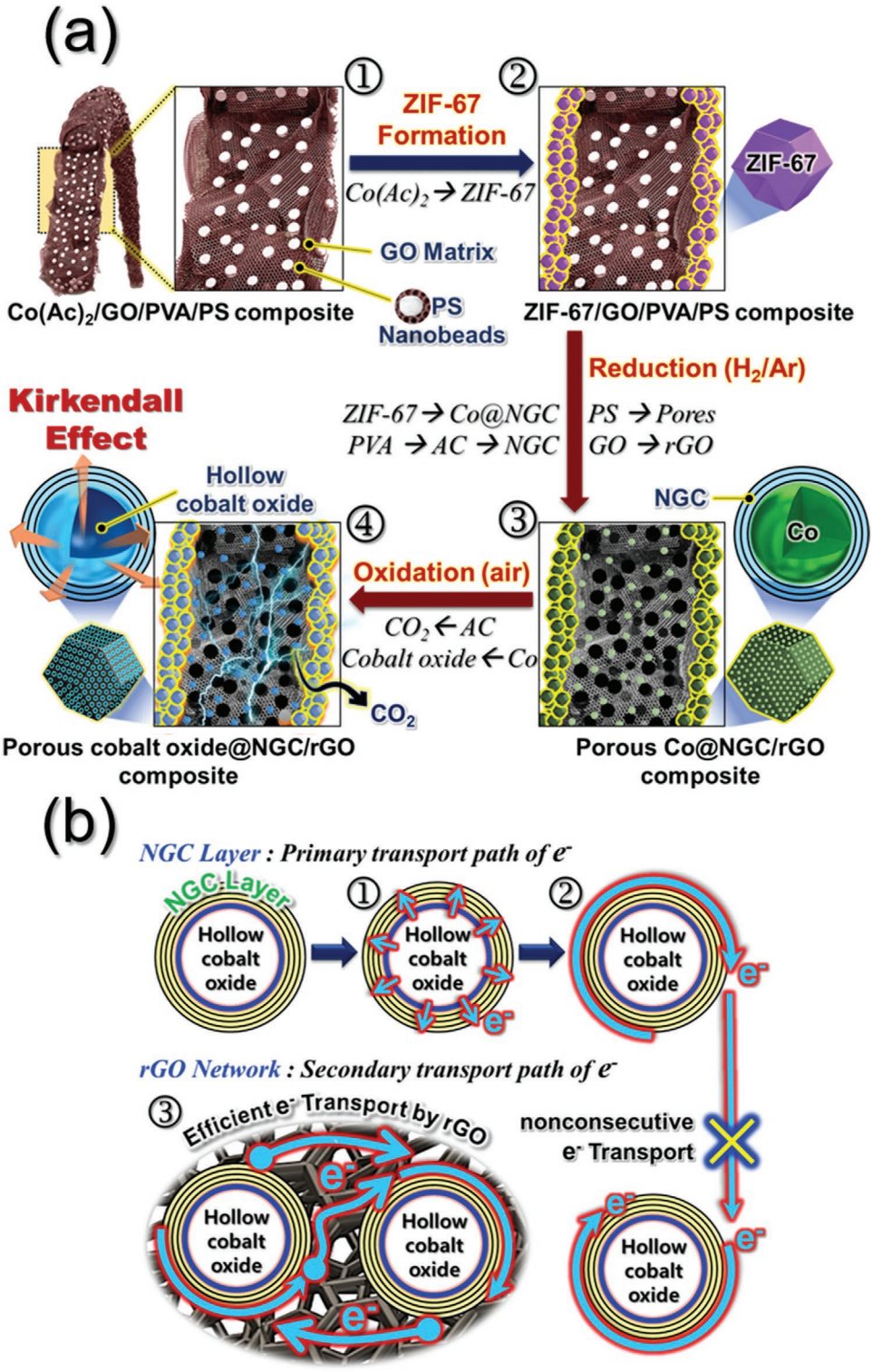

Scheme 1. a) Synthetic mechanism of the hollow cobalt oxide nanosphere/rGO composite nanofibers obtained by applying a multistep process to the electrospun nanofibers and b) efficient transport pathways for electrons by NGC coating layer and rGO network-nanofiber matrix upon Li^+ insertion and desertion process.

nanofibers as the self-engaged matrix for the growth of ZIF-67 nanocrystals are shown in Figure S1a (Supporting Information), which shows a 1D structure with a uniform diameter of ≈700 nm, smooth nanofiber surface, and solid structure from the cross-sectioned image in Figure S1b (Supporting Information). By acid treatment, the carboxylic group of the

GO dipole-dipole interacted with both PVA and PS nanobeads, resulting in fibers with highly integrated and well-distributed GO sheets in the structure. The GO in nanofibers was confirmed by Raman spectrum analysis in Figure S1c (Supporting Information), in which the broad peaks for the D-band (1360 cm^{-1}) and G-band (1600 cm^{-1}) were generally observed in the GO phase.[15,16]

To form ZIF-67 nanocrystals in nanofibers, $Co(Ac)_2$/GO/PVA/PS composite nanofibers were reacted with 2-methylimidazole, and the resulting nanofibers are shown in **Figure 1**. The nanofibers maintained their 1D structure (Figure 1a,b) and, in particular, numerous rhombic dodecahedron-shaped ZIF-67 nanocrystals with a mean size of 40 nm were generated uniformly on the nanofiber surface, as shown in Figure 1c–e. The XRD pattern (Figure 1f) indicates that the newly formed nanocrystals have typical diffraction peaks of ZIF-67 phase.[17,18] Owing to the strong coordination of 2-methylimidazole as an organic linker to cobalt ions as the metallic node in the $Co(Ac)_2$/GO/PVA/PS composite nanofibers within the methanol, uniform ZIF-67 nanocrystals were grown on the surface of the nanofibers. The elemental mapping data, shown in Figure 1g, confirmed the homogeneous distribution of elemental Co, O, C, and N all over the structure, demonstrating the uniform formation of ZIF-67 nanocrystals during the process.

The ZIF-67-composited $Co(Ac)_2$/GO/PVA/PS nanofibers were heat-treated at 400 °C in a 5% H_2/Ar mixture gas atmosphere, is shown in **Figure 2**. Even after the heat-treatment, the overall fiber structure and rhombic dodecahedron-shaped ZIF-67 nanocrystals on the nanofibers were well maintained, as shown in Figure 2a,b. Interestingly, PS nanobeads uniformly embedded between the GO sheets in the composite structure decomposed into a gaseous product to form numerous meso- and macro-pores between the GO sheets. Therefore, the well-developed porous structure could be confirmed clearly from the cross-sectioned FE-SEM images in Figure 2c and Figure S2

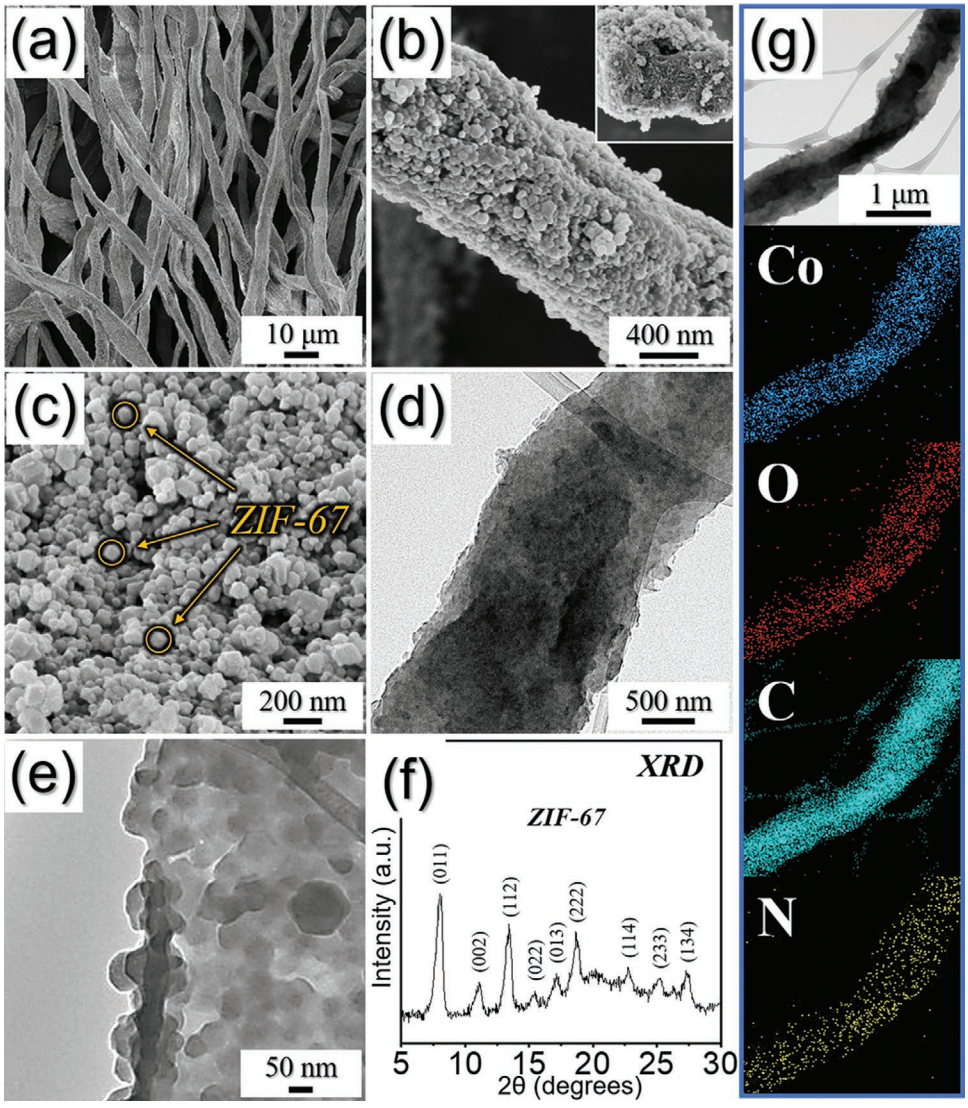

Figure 1. Morphologies, SAED pattern, and elemental mapping images of the ZIF-67 composited $Co(Ac)_2$/GO/PVA/PS nanofibers obtained after reacting as-spun fibers with 2-methylimidazole: a–c) FE-SEM images, d,e) TEM images, f) XRD pattern, and g) elemental mapping images.

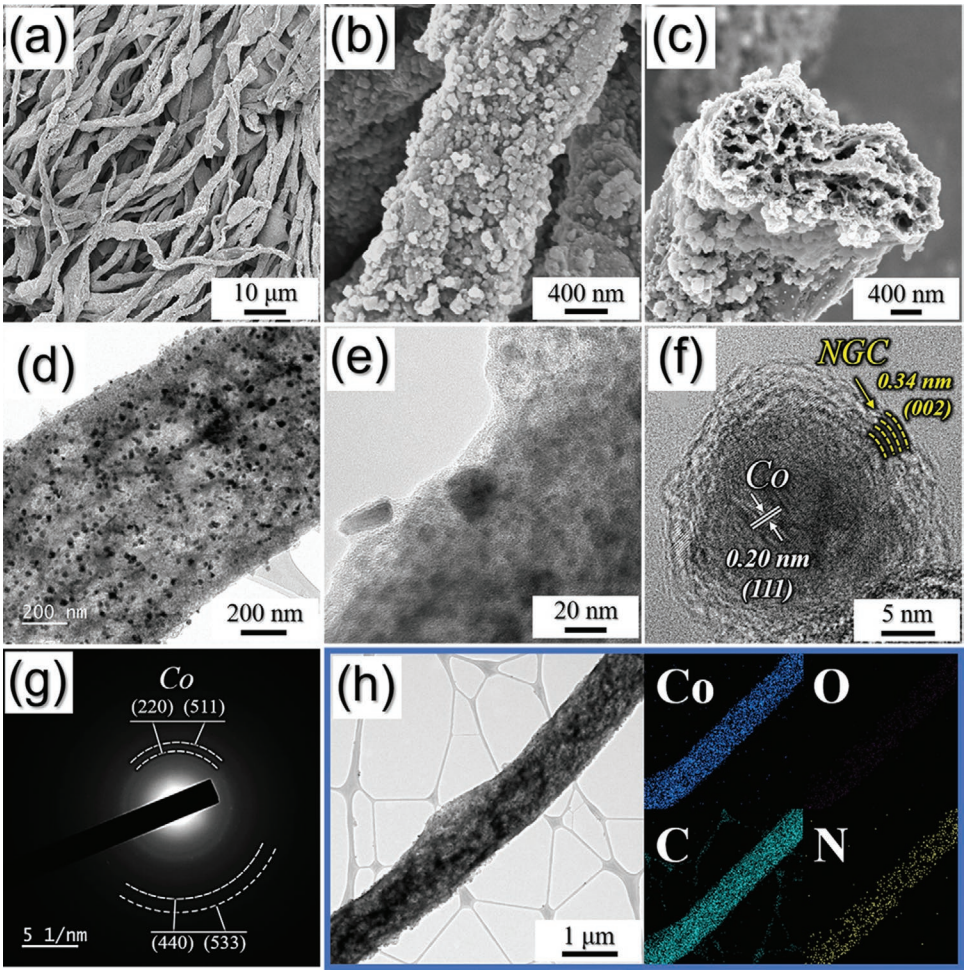

Figure 2. Morphologies, SAED pattern, and elemental mapping images of the Co@NGC/rGO composite nanofibers obtained after reduction at 400 °C: a–c) FE-SEM images, d–f) TEM images, g) SAED pattern, and h) elemental mapping images.

(Supporting Information). The pores served as channels, which could enable the efficient infiltration of reducing gas inside the structure. Hence a number of metallic Co nanocrystals with narrow-sized distribution could be embedded in the GO sheets and the carbon framework, derived by ZIF-67, as shown in the TEM images (Figure 2d,e). The high-resolution (HR)-TEM image in Figure 2f revealed that the metallic Co nanocrystal with 20 nm was coated with N-doped GC layers. During reduction, PVA initially decomposed into amorphous C, and transformed into graphitic C owing to the catalytic function of the Co metal, even at a relatively low temperature of 400 °C.[9,10] Besides, N-rich organic ligands of the ZIF-67 acted as an N-doping source, eventually doped into the GC structure to form NGC. In general, N-doped C could improve the electrical conductivity, owing to its smaller atomic radius and higher electronegativity compared with carbon.[19,20] NGC layers with clear lattice fringes separated by 0.34 nm for the (002) crystal planes of the NGC were observed in Figure 2f. Additionally, the lattice fringes separated by 0.20 nm correspond to the (110) crystal plane of the cubic metallic Co phase. Selected-area electron diffraction (SAED) (Figure 2g) and the XRD patterns in Figure S3a (Supporting Information), indicate the formation of metallic Co nanocrystals. As revealed in XRD patterns, the broad and low-intensity Co peaks demonstrate that ultrafine Co nanocrystals were successfully formed during low-temperature reduction. The additional CoO peak was due to the partial oxidation of Co nanocrystals that were exposed to air. The elemental-mapping images shown in Figure 2h further confirm the formation of Co metals uniformly coated with NGC in the rGO-matrixed nanofiber structure.

To apply the nanoscale Kirkendall diffusion mechanism, a second heat-treatment was carried out at 200, 250, or 300 °C under an air atmosphere. The conversion of metallic Co phase into cobalt oxides occurred, regardless of the oxidation temperature, which was verified by the XRD results in Figure S3b–d (Supporting Information). At the relatively low oxidation temperatures of 200 and 250 °C, binary CoO and Co_3O_4 phases were formed. However, as the temperature increased to 300 °C, only Co_3O_4 mono-phase was confirmed. The morphological changes of samples obtained after second heat-treatment as a function of oxidation temperature are shown in **Figure 3** and Figures S4 and S7 (Supporting Information). The morphologies of the S200 nanofibers obtained after the low-temperature heat-treatment at 200 °C are shown in Figure S4 (Supporting

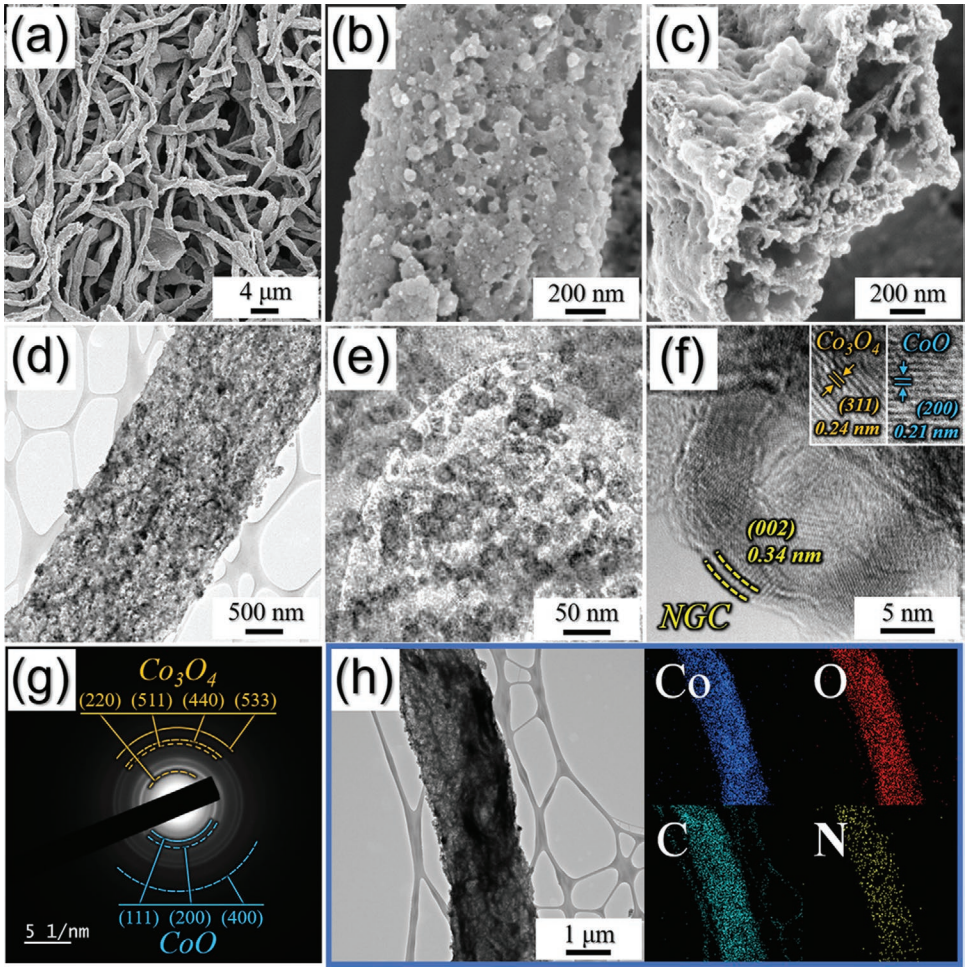

Figure 3. Morphologies, SAED pattern, and elemental mapping images of S250 nanofibers: a–c) FE-SEM images, d–f) TEM images, g) SAED pattern, and h) elemental mapping images.

Information). Similar to the nanofibers before oxidation (Figure 2), the overall porous nanofiber structure is continuously observed in Figure S4a–d (Supporting Information). However, in the HR-TEM image shown in Figure S4e (Supporting Information), the composite was constructed with many hollow nanospheres formed by the nanoscale Kirkendall diffusion process. The well-defined hollow cobalt oxide nanospheres derived from solid Co nanospheres are evidently observed in Figure S4f (Supporting Information). Additionally, it was confirmed that the NGC layer formed with the aid of the Co catalyst during the reduction process was well-coated on the nanosphere. The inset image shown in Figure S4f (Supporting Information) revealed the clear lattice fringes (0.24 nm) for (311) crystal plane of the cubic Co_3O_4 phase and the lattice fringes (0.21 nm) for (200) plane of the CoO phase. The SAED pattern shown in Figure S4h (Supporting Information) demonstrates that the S200 nanofibers were composed of binary cobalt oxide phases, which is also in good agreement with the XRD result of Figure S3b (Supporting Information). The elemental mapping images shown in Figure S4h (Supporting Information) further demonstrate that the Co particles were transformed to cobalt oxides with NGC, which were uniformly distributed in the rGO-matrixed porous nanofibers.

The morphology of the S250 nanofibers is shown in Figure 3. Porous rGO-matrixed nanofiber and the composing hollow nanospheres have morphologies similar to those of the S200 nanofibers. However, the S250 nanofibers have a lower carbon content in the composite owing to the relatively higher heat-treatment temperature. Most of the AC formed during reduction was selectively removed at the higher oxidation temperature of 250 °C, whereas the AC remained at a low temperature of 200 °C. Therefore, the ordered C materials of NGC and rGO constituted the S250 nanofibers along with the cobalt oxides. The carbon content in the S250 nanofibers, as calculated from the TGA (Figure S5b, Supporting Information) and EA (Figure S5d, Supporting Information), was 33 wt%, which is lower than that of the S200 nanofibers (43 wt%) in Figure S5a,d (Supporting Information). The N content doped in GC of the S250 nanofibers, estimated from the EA result, was ≈6.1 wt%, which is similar to that of S200 nanofibers (6.4 wt%). The NGC layers coated on the hollow cobalt oxide nanospheres were still observed, as shown in Figure 3f. The SAED pattern shown in Figure 3g revealed binary CoO and Co_3O_4 phases. The elemental mapping images in Figure 3h show the presence of cobalt oxides with NGC, and these are uniformly distributed in the rGO-matrixed porous nanofibers.

The chemical state and molecular environment of the S250 nanofibers were characterized by XPS analysis in **Figure 4**a–c and Figure S6 (Supporting Information). The survey XPS spectrum (Figure S6, Supporting Information) revealed the presence of elemental Co, O, C, and N signals. The high-resolution Co 2p XPS spectrum (Figure 4a) clearly showed two major peaks, at 780.4 for Co $2p_{3/2}$ and 795.9 eV for Co $2p_{1/2}$, with two shakeup satellites (denoted as "Sat."). [21,22] This distinctly verifies the formation of Co_3O_4. Co^{2+} species were also detected owing to the existence of the CoO phase in the structure. [23,24] The C 1s spectrum of the S250 nanofibers in Figure 4b exhibit peaks corresponding to the sp^2-bonded carbon (C–C), N-C/sp^3-bonded C–C, and C=O at 284.2, 285.1, and 288.0 eV, respectively. [25,26] Figure 4c exhibits the N 1s spectrum, which is well fitted with three peaks corresponding to the pyridinic (398.4 eV), pyrrolic (400.0 eV), and graphitic (400.9 eV) N species. [25,26] In general, the N-doped carbon enhanced the electrical conductivity and electrochemical reactivity. [19,20] Additionally, the defects formed in the N-doped carbon could provide additional Li^+ insertion sites. [27–29] Raman spectroscopy was also

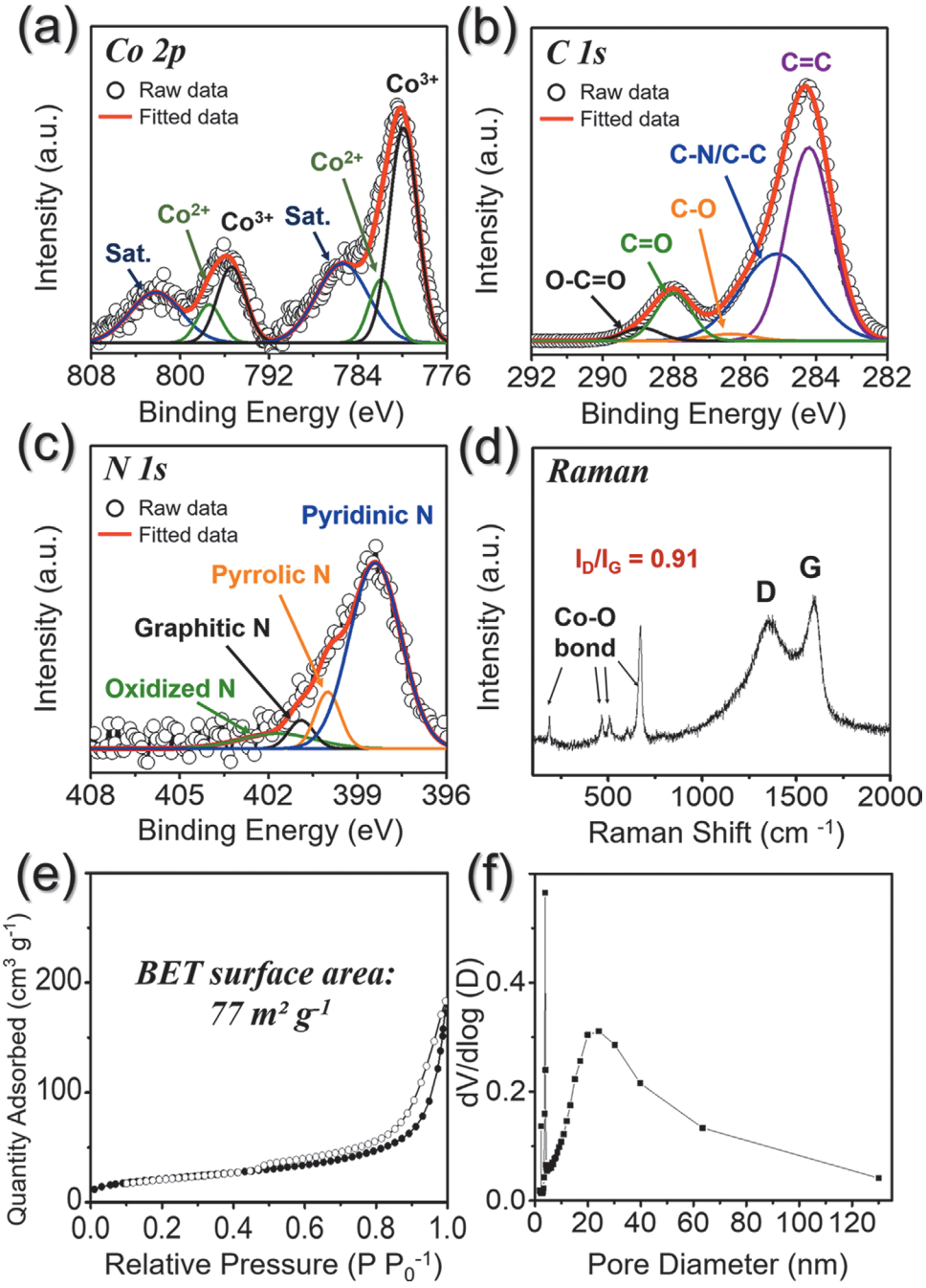

Figure 4. Characterization of S250 nanofibers: a) Co2p XPS spectrum, b) C1s XPS spectrum, c) N1s XPS spectrum, d) Raman spectrum, e) N_2 adsorption-desorption isotherms, and f) BJH desorption pore-size distribution.

employed to confirm material's electronic structure and the degree of crystallinity of C materials in Figure 4d. Four resonance peaks, at 186.9, 466.2, 506.4, and 670.1 cm^{-1}, were consistent with the typical frequencies of Co-O for cobalt oxides in the low range region.[16,30] In addition, D- (1345 cm^{-1}) and G-bands (1593 cm^{-1}) were confirmed, which generally provide useful information regarding the degree of crystallinity of the graphitic materials.[15,16] The relative intensity ratio of the D to G bands (I_D/I_G) of S250 was ≈0.81, demonstrating that the composite was composed of mainly graphitic C with high electrical conductivity. The BET surface area of the S250 nanofibers was 77 $m^2\ g^{-1}$ (Figure 4e). The Barrett–Joyner–Halenda pore size distributions in Figure 4f indicates the presence of meso- and macro-pores in the structure. Wide distributions of mesopores from 3 and 50 nm and macropores over 50 nm were formed between the rGO sheets and owing to the PS nanobead decomposition during the reduction step. Additionally, a very sharp peak at 3.8 nm is due to the tensile strength effect, based on the pore distribution curve.[31,32]

The morphologies of the S300 nanofibers are shown in Figure S7 (Supporting Information). S300 nanofibers have more macropores, compared with the S200 and S250 nanofibers, due to the combustion of both rGO and NGC at the higher temperature of 300 °C. Additionally, the cobalt oxide nanospheres constituting the fibers showed a solid structure and were aggregated with each other due to densification and sintering occurred during heat-treatment, as in Figure S7d (Supporting Information). In the TGA curve (Figure S5c, Supporting Information), no sample weight loss under an air atmosphere was observed, indicating the complete combustion of carbon during the heat-treatment process. Figure S7e (Supporting Information) revealed clear lattice fringes, separated by 0.46 nm, which correspond to the (111) crystal plane of the Co_3O_4 phase. The phase-pure Co_3O_4 with large crystallite size was only confirmed from the SAED (Figure S7f, Supporting Information) and XRD patterns (Figure S3d, Supporting Information). The elemental mapping images shown in Figure S7g (Supporting Information) also reveal the formation of carbon-free Co_3O_4 porous nanofibers. For comparison purposes, the solid-structured bare Co_3O_4 nanofibers without C were also prepared. For this, $Co(Ac)_2$/PVA fibers without GO and PS nanobeads were prepared by electrospinning in Figure S8a,b (Supporting Information). Subsequently, solid-structured bare Co_3O_4 nanofibers were obtained after heat-treatment at 600 °C under air atmosphere, as shown in Figure S8c,d (Supporting Information). The bare Co_3O_4 nanofibers with solid structure exhibited pure Co_3O_4 phase without C, which is confirmed by XRD (Figure S8e, Supporting Information) and TGA (Figure S8f, Supporting Information).

The effects of the morphological features of the hierarchical porous rGO nanofibers comprising NGC-coated hollow cobalt oxide nanospheres on their electrochemical performances as LIBs anodes were investigated, comparing those prepared at different temperatures and the bare solid Co_3O_4 nanofibers. Cyclic voltammetry (CV) curves for the initial five cycles were recorded at a scan rate of 0.1 mV s^{-1} in the voltage window 0.001–3.0 V, as shown in Figure S9 (Supporting Information). For the bare solid Co_3O_4 nanofibers, the CV curve exhibits an intense reduction peak at 0.83 V during the initial scan, which is attributed to the conversion of Co_3O_4 to Co, accompanying the formation of amorphous Li_2O and solid electrolyte interphase (SEI), which originated because of the decomposition of organic electrolyte.[33–36] During the anodic scan, a peak was observed at ≈2.05 V, which can be ascribed to the oxidation of metallic Co to Co_3O_4.[33–36] However, from the second cycle onward, the reduction peaks shifted to higher potential (≈1.03 V), owing to the formation of the ultrafine nanocrystals during the first cycle of the Co_3O_4.[37,38] Meanwhile, the CV curves of the S200 and S250 nanofibers display a slightly complex redox reaction mechanism. During the initial reduction process, S200 nanofibers exhibit a broad peak at 0.92 V, accompanied by a small shoulder peak at ≈0.74 V (marked by "*"), suggesting the biphasic/mixed-valence nature of the cobalt oxides (Co_3O_4 and CoO).[16,36] This mixed-valence nature of S200 gets more prominent for S250, indicated by the splitting of main reduction peak to two equally intense peaks. Additionally, appearance of reduction peak at 0.05 V in both S200 and S250 nanofibers suggests intercalation of Li^+ ion into the C matrix.[38,39] In the case of the S300 nanofibers, the reaction mechanism was similar to the bare solid Co_3O_4 nanofibers, because both samples were composed with pure Co_3O_4 phase. The obtained CV results are in great accordance with the XRD results (Figure S3, Supporting Information). In particular, the S250 nanofibers exhibited the smallest polarization potential (ΔV = 0.748 V), compared with S200 (ΔV = 0.816 V), S300 (ΔV = 0.973 V), and bare Co_3O_4 (ΔV = 1.046 V), which shows that the S250 nanofibers have great potential in exhibiting superior anode electrochemical performance among the samples. The hierarchical porous rGO-matrixed fiber structure and NGC coating on the hollow cobalt oxide nanospheres in the S250 nanofibers could synergically reduce the polarization potential of the sample, leading to improved electrochemical reaction kinetics. Additionally, the higher polarization potential of S200 compared with the S250 nanofibers is due to the high amount of amorphous C with relatively lower electrical conductivity in S200, which is not decomposed during heat-treatment at 200 °C in the structure.

The initial discharge and charge curves of the samples at a constant current density of 1.0 A g^{-1} are shown in **Figure 5**a. The plateau corresponding to the discharge/charge process exactly reflects the peak positions obtained from the CV curves. During charging, cells exhibit a slightly different profile; both the bare solid Co_3O_4 and S300 nanofibers display a charging plateau at 2.04 V, whereas the S200 and S250 nanofibers show a very steep charging plateau. This indicates a marginally different reaction mechanism during charging. The initial discharge capacities for the bare solid Co_3O_4 nanofibers, S200, S250, and S300 nanofibers were found to be 1133, 1520, 1631, and 1382 mAh g^{-1}, and their corresponding Coulombic efficiency (CE) values were 71%, 49%, 65%, and 75%, respectively. The initial discharge capacities of all samples are much higher than the theoretical capacity of Co_3O_4 as an anode material (≈890 mAh g^{-1}).[33–35] The extra capacity contribution may be due to the formation of a polymeric film through the decomposition of alkyl-carbonate-based electrolytes.[40,41] The relatively low CE of S200 and S 250 nanofibers were attributed to the contents of carbonaceous materials with a high initial irreversible capacity loss. The difference in voltage hysteresis mainly

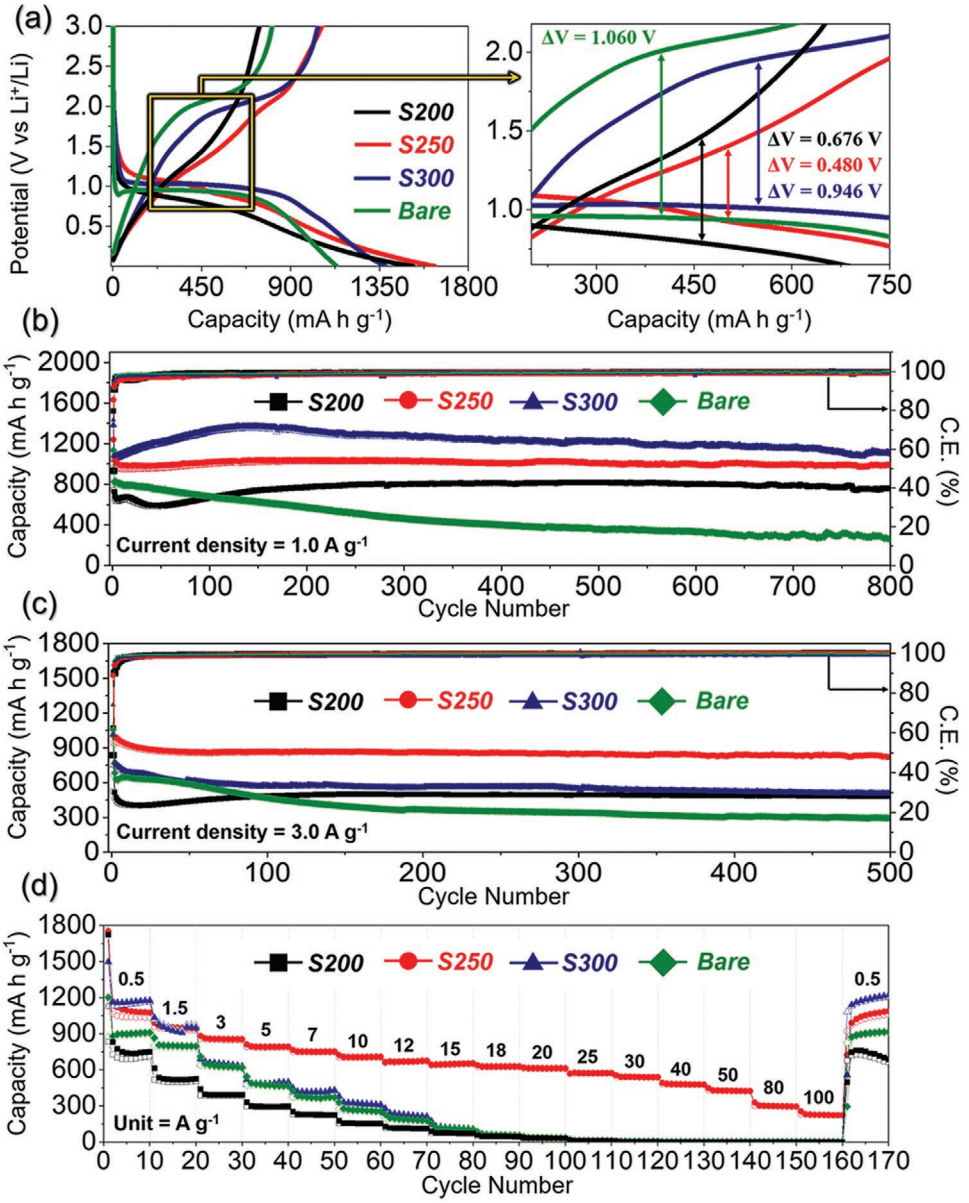

Figure 5. Electrochemical properties of the cobalt oxide nanofibers formed by multistep strategies and bare solid Co_3O_4 nanofibers formed by conventional heat-treatment process: a) initial discharge/charge curves at a constant current density of 1.0 A g^{-1}, b) cycle performances at a current density of 1.0 A g^{-1}, c) cycle performances at a current density of 3.0 A g^{-1}, and d) rate performances.

indicates the polarization potential and it was observed that the S250 nanofibers display least voltage hysteresis ($\Delta V = 0.480$ V) among all the synthesized samples. This clearly suggests that S250 nanofibers could facilitate better ionic and electron conduction, leading to great promise for high-rate LIB anodes.

Figure 5b shows the cycling performance of the nanofibers at a current density of 1.0 A g^{-1}. The bare solid Co_3O_4 nanofibers showed a continuous decrease in the capacity to 266 mAh g^{-1} after 800 cycles, because solid Co_3O_4 was collapsed by the large volume changes during the repeated cycles. However, S200, S250, and S300 showed relatively good cycle properties, regardless of the different heat-treatment temperatures, even at a high current density of 1.0 A g^{-1}. The S200, S250, and S300 nanofibers delivered reversible discharge capacities of 760, 995, and 1109 mAh g^{-1} after 800 cycles, and their corresponding CE were 99.4%, 99.5%, and 99.9%, respectively. The initial capacity increase for S200 nanofibers was observed during initial 50 cycles. The capacity increase during cycling through the formation of a polymeric gel-like film on the active material is well known for most transition-metal oxide anode materials.[42–44] Furthermore, the formation of a polymeric gel-like film over the transition-metal oxides is promoted especially by small grain and particle sizes such as S200 nanofibers.[44] Additionally, the initial capacity increase of S300 nanofibers up to ≈130 cycles was due to the pulverization of the solid Co_3O_4 nanosphere- constituting fibers, which resulted in the new generation of a fresh metal surface in each cathodic process and the formation of a continuous reversible solid electrolyte

interphase (SEI) layer.[41,45] Cycling performances under harsher conditions, a very high current density of 3.0 A g^{-1}, are also shown in Figure 5c. Compared to the performance at 1.0 A g^{-1}, only the S250 nanofibers exhibit superior cycling performance with highest reversible capacity of 823 mAh g^{-1} at the 500th cycle, even with the extremely high current density of 3.0 A g^{-1}. The capacity decay rate was found to be the lowest for the S250 nanofibers, i.e., 0.092%, compared with the bare solid Co_3O_4 (0.144%), S200 (0.118%), and S300 (0.100%) composites, indicating excellent cycling capability. comparing the cycle property particularly in high current density above 3 A g^{-1}, S250 effectively solves the kinetics problems related to the diffusion of Li^+ ions and transport of electrons during repeated charge/discharge processes, thereby resulting in superior capacities compared to other samples in the case of very high current densities. To evaluate the capacity contribution of carbon components (NGC and rGO) in the S250 nanofibers, acid treatment of S250 nanofibers with hydrochloric acid (HCl) was carried out to selectively etch cobalt oxides and, subsequently, obtain pure C fibers, which are shown in Figure S10a (Supporting Information). From the CV curves (Figure S10b, Supporting Information), the complete removal of cobalt oxides in the composite was confirmed. The pure C fibers exhibited a reversible discharge capacity of 272 mAh g^{-1} at a current density of 1.0 A g^{-1} for the 10th cycle in Figure S10c (Supporting Information). Therefore, the contribution of carbon to the discharge capacity of the S250 nanofibers could be estimated at 27%.

The rate performances of the nanofibers are shown in Figure 5d, in which the current density was increased stepwise from 0.5 to 100 A g^{-1}, then decreased to 0.5 A g^{-1}. Although, at lower current densities below 1.5 A g^{-1}, S300 nanofibers exhibit a bit higher discharge capacities among the samples, at the higher current densities above 3.0 to 100 A g^{-1}, the discharge capacity deteriorates rapidly to almost zero above 25 A g^{-1}, similar to S200 and bare solid Co_3O_4 nanofibers. In contrast, the S250 nanofibers showed substantial discharge capacities, even at an ultra-high current density, up to 100 A g^{-1}. The final discharge capacities of the S250 nanofibers at current densities of 0.5, 1.5, 3, 5, 7, 10, 12, 15, 18, 20, 25, 30, 40, 50, 80, and 100 A g^{-1} were found to be 1035, 929, 847, 787, 747, 703, 672, 650, 625, 610, 570, 537, 475, 422, 294, and 222 mAh g^{-1}, respectively. The hierarchical porous structure and NGC layer with high conductivity coated on hollow cobalt oxide nanospheres, act as a primary transport path of electrons, while rGO-nanonetwork surrounding the nanospheres, provide continuous and secondary electron transport path, that synergistically enable fast Li^+ ion and electron diffusion in the S250 nanofibers, resulting in an excellent rate performance. Moreover, when the current density was reversed to 0.5 A g^{-1}, the S250 nanofibers recovered to a capacity of 1059 mAh g^{-1}, even after extremely high current densities, indicating the high structural stability of the S250 nanofibers. The Li^+ ion storage performance of the S250 nanofibers was compared with those of the other nanostructured cobalt oxide materials and their C composites, reported in previous studies, and the results are summarized in Table S1 and Figure S11 (Supporting Information). The S250 nanofibers showed the best reversible capacities ever reported at the highest current densities and stable cycling performance, compared with those of the nanostructured cobalt oxide materials and their C hybrids with various morphologies.

To understand the excellent rate capability of S250 nanofibers, the electrochemical kinetics of the cell was investigated via CV in the voltage window of 0.001–3.0 V at different scan rates, as shown in **Figure 6**a. Subsequently, the graphs were plotted between the peak current (i) during reduction/oxidation and the scan rates (v) according to the following power-law relationship to distinguish between the capacitive-controlled and diffusion-controlled processes in the CV curves[46,47]

$$i = av^b \tag{1}$$

$$\log(i) = b\log(v) + \log(a) \tag{2}$$

where a and b are variables, whose values determine whether the process is capacitive, or diffusion controlled. For instance, if b approaches 1.0, the electrochemical reaction process is primarily controlled by the capacitive contribution.[48,49] However, if b converges to 0.5, the diffusion process dominates during the charge–discharge process. The b values are determined using the slope of the log(i) versus log(v) plots at different cathodic and anodic peaks. The calculated b values at different redox peaks for the samples are shown in Figure 6b and Figure S12 (Supporting Information). The b-values for peaks 1, 2, 3, and 4 of the S250 nanofibers were calculated at 0.85, 0.82, 0.72, and 0.83, respectively, which are close to 1.0, as shown in Figure 6b. This suggests dominant capacitive behavior during the redox process. In contrast, the S200 and S300 nanofibers in Figure S12b,f (Supporting Information) display lower b values, implying that the redox mechanism is still mainly controlled by the capacitive process but to a smaller extent. Meanwhile, bare solid Co_3O_4 nanofibers in Figure S12j (Supporting Information) exhibit the lowest b values (0.57 and 0.63 at peaks 1 and 2), which are closer to 0.5, suggesting that the dominant factor was the diffusion-controlled process during charge–discharge. Generally, the capacitive effect of the electrode material is closely related to the reaction kinetics, which means that higher the percentage of the capacitive-controlled process is, the better the transport kinetics will be and, hence, the more enhanced the rate-property of the cells will be. Therefore, for the quantitative analysis of the capacity contribution to the current response, the total stored charge in the electrode material was separated into capacitive-controlled and diffusion-limited processes, using the following equation[49]

$$i = k_1 v + k_2 v^{1/2} \tag{3}$$

where k_1v and $k_2v^{1/2}$ represent the contribution from the capacitive effect and diffusion-controlled process, respectively.[48,49] By plotting $i(V)/v^{1/2}$ versus $v^{1/2}$, constants k_1 and k_2 can be determined from the slope and intercept, respectively. Figure 6c shows the percentage of the capacitive contribution (k_1v, represented by the shaded area in red) of the S250 nanofibers at a scan rate of 10 mV s^{-1}. S250 nanofibers display the highest percentage for the capacitive process (i.e., 82%), matching well with the high b values close to 1. However, the S200, S300, and bare solid Co_3O_4 nanofibers have a lower percentage for the capacitive process (i.e., 68% for S200, 44% for S300, and 14% for bare solid Co_3O_4 nanofibers), as shown in Figure S12c,g,k (Supporting Information). The capacitive contribution of the

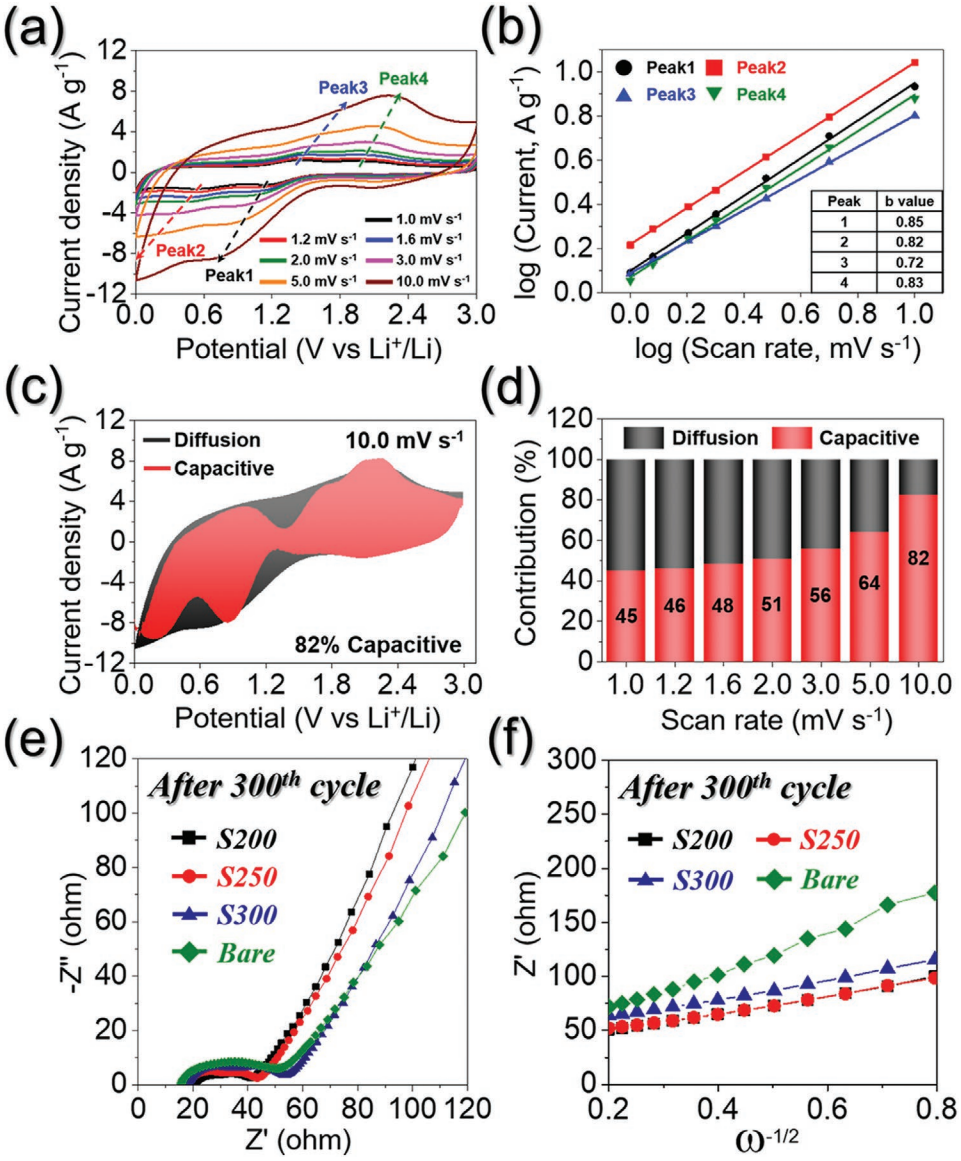

Figure 6. Electrochemical reaction dynamics analysis of S250 nanofibers: a) CV curves obtained at various scan rates, b) current response i) versus scan rate (*n*) at each redox peak, c) CV curve with the capacitive fraction shown by the red region at a scan rate of 10.0 mV s^{-1}, d) bar chart showing the percentage of the capacitive contribution at different scan rates, e) Nyquist impedance plots and f) relationships between the real part of the impedance (Z_{re}) and $\omega^{-1/2}$ of the samples obtained after 300 cycles.

S250 nanofibers was also calculated at various scan rates, as shown in Figure 6d. As can be seen, the unique hierarchical-structured S250 nanofibers deliver 45%, 46%, 48%, 51%, 56%, 64%, and 82% contribution from the capacitive effect at 1.0, 1.2, 1.6, 2.0, 3.0, 5.0, and 10.0 mV s^{-1}, respectively. The highest ratio of the capacitive-controlled contribution of the S250 nanofibers indicates relatively fast transport kinetics of Li^+ ions, which improved the rate capability of the electrodes. The rGO-network matrix and NGC coated on the hollow cobalt oxide nanospheres facilitated fast electron transfer by improving the electrical contact between the active sites of the cobalt oxide nanospheres and the electrode.

The excellent Li^+ ion storage properties of the S250 nanofibers were further verified by the EIS measurements of the cell after 300 cycles in a fully charged state, using deconvolution with a Randle-type equivalent-circuit model (Figure S13, Supporting Information), as shown in Figure 6e. The depressed semicircle in the high-medium frequency region indicates the charge transfer (R_{ct}) resistance of the cell.[37] For the R_{ct} values after the 300th cycle, both S200 and S250 nanofibers display lower impedance values (23 and 25 Ω, respectively) compared with the S300 (36 Ω) and bare solid Co_3O_4 (37 Ω) nanofibers. The results are evidence of the high electrical conductivity and structural stability of the S200 and S250 nanofibers during the repeated lithiation and delithiation processes. The porous rGO-matrixed structure and hollow cobalt oxide nanospheres coated with NGC improves the electrical conductivity and structural stability of the samples. The relationship between Z_{re} and $\omega^{-1/2}$

in the low-frequency region, where ω is the angular frequency in the low-frequency region ($\omega = 2\pi f$) is shown in Figure 6f. The less steep slopes at the low frequencies of S200 and S250 nanofibers plot indicate that the Li^+ ion diffusivity in the structure is higher than that of the S300 and bare solid Co_3O_4 nanofibers. The hierarchical porous structure composing of the rGO network matrix and cobalt oxide nanoparticles surrounded with NGC provided high Li^+ ion diffusivity in the structures. The nanostructures of the samples obtained after 300 cycles demonstrate the structure stability of the samples in **Figure 7**. The S200 and S250 nanofibers maintained their porous nanofiber structure quite well, even after repeated charge/discharge processes at an extremely high current density of 3.0 A g^{-1}, owing to their high structural stability, as shown in Figure 7a,b. Meanwhile, S300 and the bare solid Co_3O_4 nanofibers failed to withstand the internal stress because of the volume variation; therefore, they broke into several pieces and aggregated after 300 cycles in Figure 7c,d. From the results, the excellent lithium storage properties of the S250 nanofibers, including exceptional rate capability and cycling stability, were attributed to the benefits of the unique nanostructure. The unique rGO-matrixed porous structure and hollow cobalt oxide nanospheres alleviated the volume expansion during the charge/discharge process and enabled the efficient infiltration of the liquid electrolyte into the electrode. Furthermore, the NGC layer coated on the hollow cobalt oxide nanospheres, acting as a primary transport path of electrons, and the rGO-network surrounding the nanospheres provides continuous and secondary electron transport path, could synergistically enable the fast Li^+ ion and electron diffusion in the S250 nanofibers, resulting in excellent rate performance.

3. Conclusions

To obtain high-rate LIBs, we designed hierarchical porous rGO nanofibers comprising NGC-layer-coated cobalt oxide hollow nanospheres by applying the main strategies of Kirkendall diffusion effect, MOFs, and compositing with highly conductivity C to the 1D architecture. The hollow cobalt oxide nanospheres, obtained by the nanoscale Kirkendall diffusion effect, offer faster diffusion for Li^+ ion insertion/desertion than the solid ones and can better tolerate the volume variations during cycling. Furthermore, we coated NGC layers on cobalt oxide nanoparticles for the primary transport path of electrons; then the NGC-coated particles were surrounded by rGO-nanonetwork-constituting

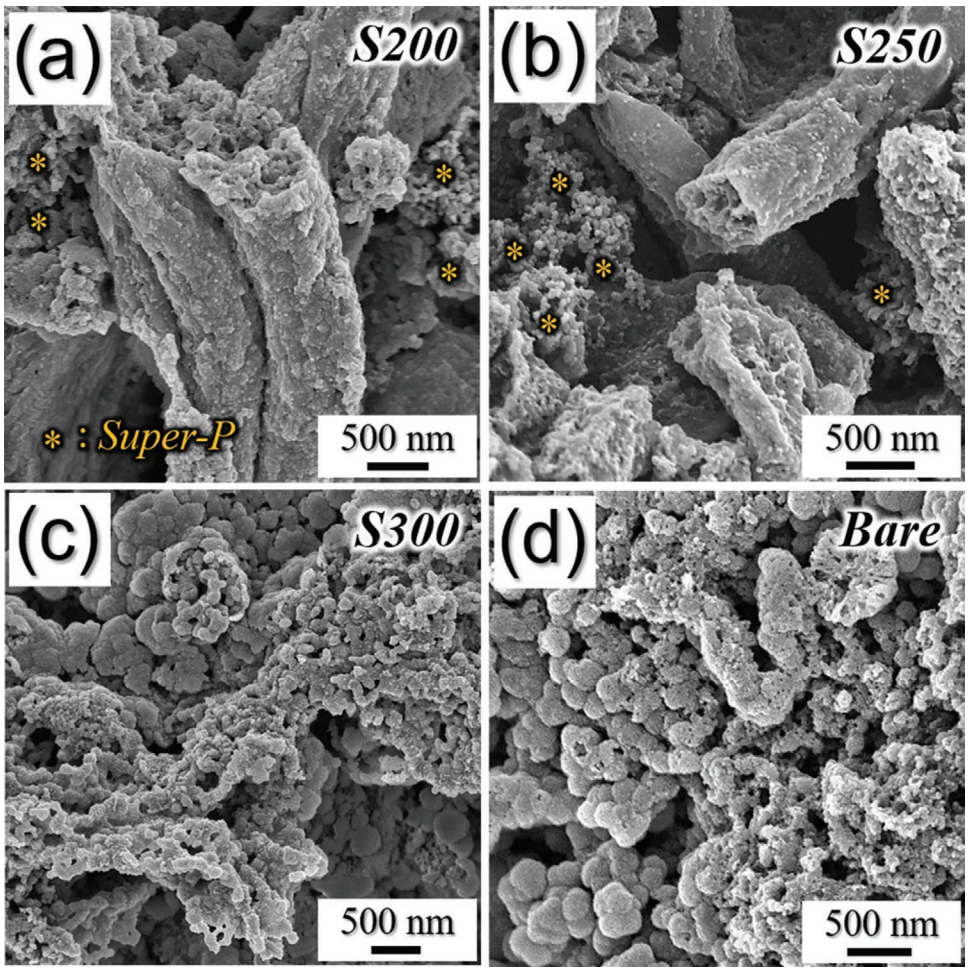

Figure 7. FE-SEM images of the nanofibers obtained after 300 cycles: a) S200, b) S250, c) S300, and d) bare solid.

nanofibers as a continuous and secondary electron transport path to the current corrector. Consequently, the synthesized S250 nanofibers exhibited high cycling and rate performance, even at extremely high current densities. The cell assembled using S250 nanofibers delivered a substantial discharge capacity of 823 mAh g^{-1} after 500 continuous cycles at an extremely high current density of 3.0 A g^{-1} with a low decay rate of 0.092% per cycle. Therefore, we believe that this nanostructure strategy has huge potential for opening new frontiers for high-rate and long-lived stable energy storage systems.

4. Experimental Section

Sample Preparation: The hierarchical porous structured rGO nanofibers comprising NGC-coated hollow cobalt oxide nanospheres were prepared by a conventional electrospinning technique and subsequent multistep process. For this, 0.5 g of graphene oxide (GO) and 2.0 g of PS nanobeads dispersed in 20 mL distilled water were added to 30 mL ethyl alcohol (Duksan, 99.9%), followed by the addition of cobalt acetate tetrahydrate ($Co(CH_3COO)_2{\cdot}4H_2O$, DaeJung Chemicals & Metals Co., Ltd., 98%) and 3.0 g of poly(vinyl alcohol) (PVA, Kanto Chemical Co. Inc., Mw: 2000) and vigorously stirred overnight. PS nanobeads with 40 nm, serving as a pore generator, were prepared by an emulsifier-free emulsion polymerization method in the previous studies.[37] GO was prepared from graphite flakes via the modified Hummers method.[50] The prepared spinning solution was loaded into a plastic syringe, equipped with a 21-gauge stainless-steel needle. The solution was ejected at a flow rate of 4 mL h^{-1} onto a drum collector covered with Al foil. During the electrospinning process, the distance between the tip and the collector was fixed at 15 cm and the rotation speed of the drum collector was at 180 rpm. The applied voltage between the collector and needle tip was 20 kV. The as-spun $Co(Ac)_2$/GO/PVA/PS composite nanofibers were stabilized in an air atmosphere at 100 °C. Subsequently, 0.5 g of stabilized $Co(Ac)_2$/GO/PVA/PS composite nanofibers was added into 50 mL of methanol solution with 3.0 g of 2-methylimidazole (Wako Pure Chemical Industries, Ltd., 98%) and then kept at 20 °C for 24 h to form ZIF-67 nanocrystals on $Co(Ac)_2$/GO/PVA/PS composite nanofibers. Subsequently, the initial heat-treatment for reduction was conducted at 400 °C for 3 h at a heating rate of 5 °C min^{-1} under 5% H_2/Ar mixture gas atmosphere. The second heat-treatment for oxidation was conducted at temperatures of 200, 250, and 300 °C for 3 h at a heating rate of 5 °C min^{-1} in an air atmosphere. For simplicity, the nanofibers obtained after the second heat-treatment at 200, 250, and 300 °C are referred to as "S200," "S250," and "S300" nanofibers, respectively. For comparison, bare Co_3O_4 nanofibers with a filled structure were also prepared. For this preparation, $Co(Ac)_2$/PVA as-spun fibers without GO and PS nanobeads were prepared via electrospinning. Subsequently, bare Co_3O_4 solid nanofibers without C were finally obtained after heat-treatment at 600 °C for 3 h in an air atmosphere.

Characterization: The morphological features of the nanofibers were investigated using field-emission scanning electron microscopy (FE-SEM, ULTRA PLUS, ZEISS) and field-emission transmission electron microscopy (TEM, JEOL, JEM-2100F). The crystal structures were investigated via X-ray diffraction (XRD) analysis (D8 Discover with GADDS, Bruker) using Cu K_α radiation (λ = 1.5418 Å). X-ray photoelectron spectroscopy (XPS) was performed using a Thermo Scientific K-Alpha spectrometer with Al Kα radiation to analyze the chemical compositions of the samples. A structural investigation of the C content in the sample was performed using Raman spectroscopy (LabRam HR800, Horiba Jobin-Yvon, excited by a 515 nm diode laser at 25 °C). The surface areas of the samples were measured using the Brunauer–Emmett–Teller (BET) method, where N_2 was used as the adsorbate gas. Thermogravimetric analysis (TGA) was performed using a Pyris 1 thermogravimetric analyzer (Perkin Elmer) in the temperature range of 25–700 °C at a heating rate of 10 °C min^{-1} in air.

Electrochemical Measurements: The electrochemical properties of the nanofibers were measured by fabricating 2032-type coin cells. The cell electrode was prepared by mixing 70 wt% active material, 20 wt% carbon black (Super-P) as a conductive material, and 10 wt% sodium carboxymethyl cellulose (CMC) as a binder. Lithium metal and a microporous polypropylene film were used as the counter electrode and separator, respectively. The electrolyte was prepared by dissolving 1 M $LiPF_6$ in a 1:1 v/v mixture of fluoroethylene carbonate and dimethyl carbonate (FEC/DMC). The coin cell was assembled in an argon atmosphere in a glove box. The discharge–charge characteristics of the samples were measured at various current densities in the voltage range of 0.001–3.0 V. Cyclic voltammetry measurements were performed at a scan rate of 0.1 mV s^{-1}. The electrochemical impedance was measured by electrochemical impedance spectroscopy (EIS) over a frequency range of 100 kHz to 10 mHz with a signal amplitude of 10 mV.

Supporting Information

Supporting Information is available from the Wiley Online Library or from the author.

Acknowledgements

This work was supported by the National Research Foundation of Korea (NRF). The grant was funded by the government of Korea (MSIP) (NRF-2018R1A4A1024691, NRF-2017M1A2A2087577, and NRF-2018R1D1A3B07042514).

Conflict of Interest

The authors declare no conflict of interest.

Keywords

anode materials, graphene, lithium-ion batteries, metal–organic frameworks, transition metal oxide

Received: April 6, 2020
Revised: May 22, 2020
Published online: July 2, 2020

[1] J. S. Cho, J. M. Won, J.-K. Lee, Y. C. Kang, *Nano Energy* **2016**, *26*, 466.
[2] C. He, S. Wu, N. Zhao, C. Shi, E. Liu, J. Li, *ACS Nano* **2013**, *7*, 4459.
[3] C. Peng, B. Chen, Y. Qin, S. Yang, C. Li, Y. Zuo, S. Liu, J. Yang, *ACS Nano* **2012**, *6*, 1074.
[4] P. Roy, S. K. Srivastava, *J. Mater. Chem. A* **2015**, *3*, 2454.
[5] H. Nakajima, *JOM* **1997**, *49*, 15.
[6] Y. Hu, X. Huang, K. Wang, J. Liu, J. Jiang, R. Ding, X. Ji, X. Li, *J. Solid State Chem.* **2010**, *183*, 662.
[7] F. Li, Q.-Q. Zou, Y.-Y. Xia, *J. Power Sources* **2008**, *177*, 546.
[8] J.-W. Wen, D.-W. Zhang, Y. Zang, X. Sun, B. Cheng, C.-X. Ding, Y. Yu, C.-H. Chen, *Electrochim. Acta* **2014**, *132*, 193.
[9] S.-K. Park, J. K. Kim, J. H. Kim, Y. C. Kang, *Mater. Charact.* **2017**, *132*, 320.
[10] C.-L. Zhang, B.-R. Lu, F.-H. Cao, Z.-L. Yu, H.-P. Cong, S.-H. Yu, *J. Mater. Chem. A* **2018**, *6*, 12962.
[11] J. Zhang, L. Yu, X. W. D. Lou, *Nano Res.* **2017**, *10*, 4298.
[12] C. Sun, J. Yang, X. Rui, W. Zhang, Q. Yan, P. Chen, F. Huo, W. Huang, X. Dong, *J. Mater. Chem. A* **2015**, *3*, 8483.

[13] K. Zhao, L. Zhang, R. Xia, Y. Dong, W. Xu, C. Niu, L. He, M. Yan, L. Qu, L. Mai, *Small* **2016**, *12*, 588.
[14] W.-M. Zhang, X.-L. Wu, J.-S. Hu, Y.-G. Guo, L.-J. Wan, *Adv. Funct. Mater.* **2008**, *18*, 3941.
[15] A. C. Ferrari, J. Meyer, V. Scardaci, C. Casiraghi, M. Lazzeri, F. Mauri, S. Piscanec, D. Jiang, K. Novoselov, S. Roth, *Phys. Rev. Lett.* **2006**, *97*, 187401.
[16] Y. Qi, H. Zhang, N. Du, D. Yang, *J. Mater. Chem. A* **2013**, *1*, 2337.
[17] J. Qian, F. Sun, L. Qin, *Mater. Lett.* **2012**, *82*, 220.
[18] K. Zhou, B. Mousavi, Z. Luo, S. Phatanasri, S. Chaemchuen, F. Verpoort, *J. Mater. Chem. A* **2017**, *5*, 952.
[19] Y. Cheng, L. Huang, X. Xiao, B. Yao, L. Yuan, T. Li, Z. Hu, B. Wang, J. Wan, J. Zhou, *Nano Energy* **2015**, *15*, 66.
[20] S. Y. Jeong, S. Ghosh, J.-K. Kim, D.-W. Kang, S. M. Jeong, Y. C. Kang, J. S. Cho, *J. Ind. Eng. Chem.* **2019**, *75*, 100.
[21] X. Wang, W. Li, X. Wang, J. Zhang, L. Sun, C. Gao, J. Shang, Y. Hu, Q. Zhu, *RSC Adv.* **2017**, *7*, 50753.
[22] N. Yan, L. Hu, Y. Li, Y. Wang, H. Zhong, X. Hu, X. Kong, Q. Chen, *J. Phys. Chem. C* **2012**, *116*, 7227.
[23] Y. Xiao, C. Hu, M. Cao, *J. Power Sources* **2014**, *247*, 49.
[24] X. Zhou, Y. Zhong, M. Yang, Q. Zhang, J. Wei, Z. Zhou, *ACS Appl. Mater. Interfaces* **2015**, *7*, 12022.
[25] S.-K. Park, J. K. Kim, Y. C. Kang, *Chem. Eng. J.* **2017**, *328*, 546.
[26] S.-K. Park, J.-S. Park, Y. C. Kang, *J. Mater. Chem. A* **2018**, *6*, 1028.
[27] J. Dong, Y. Xue, C. Zhang, Q. Weng, P. Dai, Y. Yang, M. Zhou, C. Li, Q. Cui, X. Kang, *Adv. Mater.* **2017**, *29*, 1603692.
[28] J. Hou, C. Cao, F. Idrees, X. Ma, *ACS Nano* **2015**, *9*, 2556.
[29] L. Qie, W. M. Chen, Z. H. Wang, Q. G. Shao, X. Li, L. X. Yuan, X. L. Hu, W. X. Zhang, Y. H. Huang, *Adv. Mater.* **2012**, *24*, 2047.
[30] V. Hadjiev, M. Iliev, I. Vergilov, *J. Phys.: Condens. Matter* **1988**, *21*, L199.
[31] H. Du, L. Jiao, Q. Wang, Q. Huan, W. Peng, D. Song, Y. Wang, H. Yuan, *J. Power Sources* **2011**, *196*, 10748.
[32] J. C. Groen, L. A. Peffer, J. Pérez-Ramírez, *Microporous Mesoporous Mater.* **2003**, *60*, 1.
[33] N. Jayaprakash, W. D. Jones, S. S. Moganty, L. A. Archer, *J. Power Sources* **2012**, *200*, 53.
[34] X. Leng, S. Wei, Z. Jiang, J. Lian, G. Wang, Q. Jiang, *Sci. Rep.* **2015**, *5*, 16629.
[35] F. Wang, D. Cheng, W. Wang, Y. Wang, M. Zhao, S. Yang, X. Lu, X. Song, *RSC Adv.* **2015**, *5*, 23326.
[36] M. Reddy, G. Prithvi, K. P. Loh, B. Chowdari, *ACS Appl. Mater. Interfaces* **2014**, *6*, 680.
[37] M. S. Jo, S. Ghosh, S. M. Jeong, Y. C. Kang, J. S. Cho, *Nano-Micro Lett.* **2019**, *11*, 3.
[38] S. Klink, E. Ventosa, W. Xia, F. La Mantia, M. Muhler, W. Schuhmann, *Electrochem. Commun.* **2012**, *15*, 10.
[39] G. Gao, Y. Jin, Q. Zeng, D. Wang, C. Shen, *Beilstein J. Nanotechnol.* **2017**, *8*, 649.
[40] J. Bai, X. Li, G. Liu, Y. Qian, S. Xiong, *Adv. Funct. Mater.* **2014**, *24*, 3012.
[41] L. Su, Y. Zhong, Z. Zhou, *J. Mater. Chem. A* **2013**, *1*, 15158.
[42] Z.-S. Wu, W. Ren, L. Wen, L. Gao, J. Zhao, Z. Chen, G. Zhou, F. Li, H.-M. Cheng, *ACS Nano* **2010**, *4*, 3187.
[43] G. Zhou, D.-W. Wang, F. Li, L. Zhang, N. Li, Z.-S. Wu, L. Wen, G. Q. Lu, H.-M. Cheng, *Chem. Mater.* **2010**, *22*, 5306.
[44] J.-S. Do, C.-H. Weng, *J. Power Sources* **2005**, *146*, 482.
[45] J. S. Cho, J.-S. Park, Y. C. Kang, *Nano Res.* **2017**, *10*, 897.
[46] H. Kim, K. Lim, G. Yoon, J. H. Park, K. Ku, H. D. Lim, Y. E. Sung, K. Kang, *Adv. Energy Mater.* **2017**, *7*, 1700418.
[47] K. Zhang, M. Park, L. Zhou, G. H. Lee, W. Li, Y. M. Kang, J. Chen, *Adv. Funct. Mater.* **2016**, *26*, 6728.
[48] S. Y. Jeong, J. S. Cho, *Nanomaterials* **2019**, *9*, 1362.
[49] J. K. Kim, S.-K. Park, J.-S. Park, Y. C. Kang, *J. Mater. Chem. A* **2019**, *7*, 2636.
[50] G. D. Park, J. S. Cho, Y. C. Kang, *ACS Appl. Mater. Interfaces* **2015**, *7*, 16842.